

DOE/ET-53088-337

IFSR #337

**A Fluid-Ion and Particle-Electron Model
for Low-Frequency Plasma Instabilities[†]**

*P.M. Lyster**

Institute for Fusion Studies
The University of Texas at Austin
Austin, Texas 78712 and

J-N. Leboeuf

Oak Ridge National Laboratory
Fusion Energy Division
Oak Ridge, TN 37830

January 1992

[†] *IFS Report, May, 1990/Accepted for publication, J. Comput. Phys., April, 1991*

^{*} *Present address: Jet Propulsion Lab, Pasadena, CA 91109*

A Fluid-Ion and Particle-Electron Model for Low-Frequency Plasma Instabilities

P.M. Lyster*

Institute for Fusion Studies
The University of Texas at Austin
Austin, Texas 78712

and

J.-N. Leboeuf
Oak Ridge National Laboratory
Fusion Energy Division
Oak Ridge, Tennessee 37830

Categories: 65C20 Numerical Simulation
(Models, Numerical Methods)
77xx PLASMA PHYSICS
77F05 Fluid-Particle models

January 3, 1992

IFSR No. 337 This paper was accepted for publication in J. Comput. Phys, April 1991.

*Present address: Jet Propulsion Laboratory, 4800 Oak Grove Drive, Pasadena, CA 91109

Abstract

We have developed a hybrid (particle/fluid) computer code for the study of quasi-neutral micro-instabilities for inhomogeneous plasmas that are immersed in a magnetic field. The ions are treated in the fluid approximation, retaining perpendicular $\mathbf{E} \times \mathbf{B}$ and polarization drifts as well as the parallel momentum and ion temperature equations. The electrons are represented as particles with perpendicular $\mathbf{E} \times \mathbf{B}$ drifts and parallel kinetics, thus exactly describing the effects of trapped electrons and electron-wave resonances. The code may be used in the study of low frequency ($\omega < \Omega_i$ where $\Omega_i = eB/m_i c$) universal mode drift waves, ion-pressure-driven modes, or curvature-driven modes. At present we have implemented an electrostatic, two-dimensional, slab geometry version of the code. The model has been tested extensively for sound-wave propagation, the collisionless (universal mode) drift wave real frequency and growth rate, the η_i -mode real frequency and growth rate, and the fluctuation spectrum has been elucidated. As a nonlinear test case, we have also studied the nonlinear properties of the collisionless drift wave.

1. Introduction

The expression “hybrid code” has come to refer to the use of both particle and fluid simulation models in a single computer code [1–6]. In plasma physics such a technique follows naturally from the fact that plasmas are composed of a number of different charged species; at the most basic level there are electrons present and one species of ion. The large mass ratio $m_p/m_e = 1836$ between protons and electrons contributes to the presence of diverse temporal and spatial scales in the plasma. Ignoring for the moment issues relating to the propagation of electromagnetic radiation, the smallest length is the Debye length $\lambda_D = \sqrt{T_e/4\pi n e^2}$ in cgs units, where T_e is the electron temperature and n is the electron number density, and the highest frequency is the plasma frequency $\omega_e = \sqrt{4\pi n e^2/m_e}$. The most natural form of hybrid model is to treat the electrons as a fluid and the ions as particles. This removes kinetic wave-particle electron effects and also removes the $1/\sqrt{N_e}$ noise component, where N_e is a number of electron macroparticles. This allows for further simplifications: in a sufficiently collisional plasma a simple Ohm’s law may be used, or the electron inertia may be neglected in the electron momentum equation. These approximations along with the imposition of quasi-neutrality $n_p = n_e$ eliminate scales of order λ_D and ω_e [1]. Also, the neglect of the electron mass further removes scales of the electron Larmor radius $\rho_e = v_e/\Omega_e$, where v_e is the electron thermal velocity and $\Omega_e = eB/m_e c$ is the electron cyclotron frequency. Furthermore, the Darwin approximation [2] may be imposed whereby the transverse displacement current is neglected and the speed of light on the grid ceases to impose problems of numerical stability [2,3,4,5]. There are a number of realizations of the particle-ion and fluid-electron approach. For example, the massless electron model has been exploited by Hewett [3], Harned [4], and Mankofsky *et al.* [5]. Another example is the quasi-neutral Darwin model due to Hewett and Nielson [6] that retains finite electron mass in the longitudinal component of Ohm’s law. There are techniques, other than hybrid codes, for increasing the time and space scales

of simulations: implicit or time filtering schemes, orbit averaging and subcycling (many of which are discussed in the book “Multiple Timescales” [7]), and the gyrokinetic approach [8] which is based on physical equations that have been averaged over the ion gyroperiod.

Our hybrid model, first proposed by Okuda [9], represents the electrons as particles and the ions as fluid. Okuda has sketched out the model, and we have coded it up as well as analyzed and tested its behavior. For the relevant modes, quasi-neutrality over scales longer than the Debye length is assumed, the typical frequency ω is taken to be much smaller than the ion Larmor frequency $\Omega_i = eB/m_p c$, and the wavelength λ long compared with the ion Larmor radius $\rho_i = v_i/\Omega_i$. Our model retains the electron particle equation of motion in the direction parallel to an ambient magnetic field. We assume a vanishingly small electron Larmor radius so that the perpendicular guiding center motion in two-dimensional slab geometry can be handled with $\mathbf{E} \times \mathbf{B}$ drifts. The magnetic field gradients are small so that the gradient- B drifts are negligible. We have also as yet not included curvature drifts in our model. This model is similar to that of Lee and Okuda [10] who treat the ions fully kinetically. It is also similar to the approach of D’Ippolito *et al.* [11] who represent the electrons in the same way as we do, but use a full Vlasov treatment of the ions. Our model is at present electrostatic, although we are aware of work in progress to make a similar electromagnetic model [12].

The treatment of the ions is essentially the same as in reduced magnetohydrodynamics [13], so the new feature here is the representation of the electrons as particles. This may be used for cases where electron kinetic effects, such as parallel wave particle resonances, or trapped particles are important, while the ion response is fluid-like. In cases where ion Landau damping is important, this may be approximated using artificial viscosity. However, accurate treatment of ion Landau damping or trapped ion modes in complicated geometry, or the complete finite Larmor radius treatment of the ions are not included in this model.

In the following section the electrostatic model equations are described and the numerical algorithm outlined. Section 3 describes extensive tests that were made to verify sound wave

propagation, the real and imaginary frequency dispersion relations for the collisionless drift wave (universal mode) and η_i -mode drift wave, and also the fluctuation spectrum properties of the code are elucidated. Finally, in Section 4 we consider the nonlinear drift wave instability. Drift waves have been studied computationally using both kinetic [14] and fluid [15] treatments. In our case we compare the results between the hybrid model and a full dynamics ion model for the case of the collisionless drift wave instability.

2. Model Equations and Algorithm

The ions in the model are treated in the same way as for reduced magnetohydrodynamics [13,16]. Our equations follow closely from Horton *et al.* [17], as well as from references [18, 19, 20, 21]. In the electrostatic case where quasineutrality is assumed, the fluid equations are

$$\rho_s^2 \nabla_\perp \cdot n_0 (\partial_t + \mathbf{v}_{Di} \cdot \nabla) \nabla_\perp \left(\frac{e\varphi}{T_e} \right) = \nabla_\parallel n (v_{\parallel e} - v_{\parallel i}) \quad (1)$$

$$m_i n \left(\partial_t + (\mathbf{v}_E + v_{\parallel i} \hat{\mathbf{b}}) \cdot \nabla \right) v_{\parallel i} = -en \nabla_\parallel \varphi - \nabla_\parallel P_i \quad (2)$$

$$\frac{3}{2} \left(\partial_t + (\mathbf{v}_E + \mathbf{v}_{\parallel i} \hat{\mathbf{b}}) \cdot \nabla \right) T_i + T_i \nabla_\parallel v_{\parallel i} = 0, \quad (3)$$

where $n_i = n_e = n$, and n_0 is the unperturbed density, φ is the electrostatic potential (cgs units), $v_{\parallel i}$ and $v_{\parallel e}$ are the respective ion and electron velocities parallel to the magnetic field direction $\hat{\mathbf{b}} = \mathbf{B}/B$, the electron velocity will be obtained by averaging electron particle velocities. The electron and ion temperatures are T_e and T_i , while $P_i = nT_i$. Also, $\rho_s = c_s/\Omega_i$, $c_s = \sqrt{T_e/m_i}$ and the perpendicular velocities are

$$\mathbf{v}_E = \frac{c}{B} \hat{\mathbf{b}} \times \nabla \varphi \quad (4)$$

$$\mathbf{v}_{Di} = \mathbf{v}_E + \frac{c}{eBn} \hat{\mathbf{b}} \times \nabla P_i. \quad (5)$$

In equation (1) only the dominant convective nonlinearity is retained. This equation represents the charge balance that maintains quasineutrality. In the low frequency regime $\omega < \Omega_i$, the ions perform $\mathbf{E} \times \mathbf{B}$ as well as polarization drifts in the perpendicular direction. The latter is responsible for a charge separation which is cancelled by the parallel motion of the ions and electrons.

Horton *et al.* [17] assumed Boltzmann electrons, that is $\delta n_e = n_0(e\varphi/T_e)$, however in our model the electrons are treated as macroparticles. The parallel dynamics are followed using the single particle equation of motion, and the perpendicular velocity is $(c\mathbf{E} \times \mathbf{B}/B^2)$ [10].

$$m_e \frac{d}{dt} \mathbf{v}_{\parallel q} = e \nabla_{\parallel} \varphi(\mathbf{x}_q) , \quad (6)$$

$$\mathbf{v}_{\perp q} = \frac{c}{B} \hat{\mathbf{b}} \times \nabla \varphi(\mathbf{x}_q) , \quad (7)$$

$$\frac{d}{dt} \mathbf{x}_q = \mathbf{v}_{\perp q} + \mathbf{v}_{\parallel q} \quad (8)$$

where the subscript q refers to individual particles. The electron parallel velocity moment and the density that are needed in Eqs. (1) and (2) are evaluated using the subtracted dipole method [22]. In generalized notation

$$n(\mathbf{x}_G) v_{\parallel e}(\mathbf{x}_G) = \sum_q v_{\parallel q} S(\mathbf{x}_G - \mathbf{x}_q) \quad (9)$$

and

$$n(\mathbf{x}_G) = \sum_q S(\mathbf{x}_G - \mathbf{x}_q) \quad (10)$$

where S is the particle-grid weighting function, and \mathbf{x}_G is a grid-point position. The field equations (1)–(3) can then be solved for on a spatial grid.

The geometry is sheared slab. Figure 1 shows a schematic with the “radial” coordinate in usual Tokamak geometry taken to be in the x -direction. The scale lengths for the zero order density and ion-temperature profiles are L_n and L_T respectively. When considering modes driven by ion-temperature-gradient (η_i -mode), the quantity $\eta_i = L_n/L_T$ is defined in order

to parameterize the the relative scales. The magnetic field is at an angle $\theta(x)$ in units radian to the z -axis; when we refer to the shearless case, θ is taken to have no x -dependence. Also, when we refer to the one-dimensional version of the code, only variations in the y -direction are retained. The two-dimensional version has variations in x and y , while for both of the realizations $k_{\parallel} = k_{\perp} \tan \theta$.

We have normalized Eqs. (1), (2), (3), (6), and (7) according to the following procedure: $t' = \omega_e t$, $\mathbf{x}' = \mathbf{x}/\Delta$ (where Δ is the finite-difference grid spacing), $n' = n/n_0$, $\mathbf{E}' = (e/m_e \omega_e^2 \Delta) \mathbf{E}$, $\varphi' = (e/m_e \omega_e^2 \Delta^2) \varphi$, $\mathbf{B}' = e \mathbf{B}/(m_e c \omega_e)$, $v'_{\parallel i} = v_{\parallel i}/\omega_e \Delta$, and $T'_i = T_i/m_e \omega_e^2 \Delta^2$. In the new variables (without the primes) the vorticity ($U = \nabla_{\perp}^2 \varphi$), parallel ion momentum, and the ion temperature equations can be rewritten

$$\partial_t U = -\frac{\cos \theta}{B} [\varphi + P, U] - \frac{\cos \theta}{B} [\partial_x P, \partial_x \varphi] - \frac{\cos^3 \theta}{B} [\partial_y P, \partial_y \varphi] + \left(\frac{m_e}{m_i}\right) B^2 \nabla_{\parallel} n (v_{\parallel i} - v_{\parallel e}) \quad (11)$$

$$\partial_t v_{\parallel i} = -\frac{\cos \theta}{B} [\varphi, v_{\parallel i}] - \nabla_{\parallel} v_{\parallel i}^2 / 2 - \left(\frac{m_e}{m_i}\right) \nabla_{\parallel} \varphi - \left(\frac{m_e}{m_i}\right) \nabla_{\parallel} P \quad (12)$$

$$\partial_t T_i = -\frac{\cos \theta}{B} [\varphi, T_i] - v_{\parallel i} \nabla_{\parallel} T_i - \frac{2}{3} T_i \nabla_{\parallel} v_{\parallel i} \quad (13)$$

where $\nabla_{\parallel} \equiv \sin \theta \frac{\partial}{\partial y}$, $[f, g] = (\partial_x f \partial_y g - \partial_y f \partial_x g)$, $P = n T_i$ and $\tau = T_e/T_i$. These equations closely resemble the electrostatic version of the four-field model of reduced magnetohydrodynamics [16]. The second and third terms in the vorticity equation, Eq. (11), arise from the spatial variation of the diamagnetic drift, and are neglected here. In Eq. (11) the linear contribution due to the presence of external density and temperature gradients comes from the Poisson bracket $-(\cos \theta/B)[P, U]$; this contributes a term $(v_D/\tau)(1 + \eta_i) \cos \theta \partial_y U$, where $v_D = T_e/(BL_n)$ in normalized units. In Eq. (13) the bracket $-(\cos \theta/B)[\varphi, T_i]$ contributes a term $-(v_D/\tau) \eta_i \cos \theta \partial_y \varphi$.

We now present an outline of the algorithm that is employed. The time advance is performed in two steps, the first of which calculates quantities at a half timestep so that they may be used to advance the equations in a time-centered way. Therefore, the implementation

is second order accurate in time. Start off with $U^{n+1/2}$, $\varphi^{n+1/2}$, $v_{\parallel i}^{n+1/2}$, and $T_i^{n+1/2}$ for the ions, and $v_{\parallel q}^n$ and $\mathbf{x}_q^{n+1/2}$ for the electrons; the superscript fixes the time level where $t = n\Delta t$ and Δt is the code timestep. The algorithm is finite-difference in space as well as time, however, the vorticity is inverted using a fast Fourier transform (FFT) to obtain φ . All of the perturbed quantities are periodic in the x - and y -directions, and they are solved for on a common grid, that is, there are no interleaving meshes. We have used the subtracted dipole particle interpolation scheme [22], and this is known to have discontinuities in the effective particle weight function S . To reduce the resulting noise in the calculation of φ from the velocity moments we employ a spatial filter. Since the FFT is used to invert the vorticity we perform the filtering in Fourier space using a form factor $e^{-k_{\perp}^2 a^2}$. In all of our work presented here we have taken $a = 1.5\Delta$, that is, we strongly filter only the highest k_{\perp} modes. Note that this does not affect the resolution of wave-particle resonances for which $k_{\parallel} v_e \Delta t < 1$ (v_e is the electron parallel thermal velocity) since the corresponding perpendicular wavenumbers $k_{\perp} = k_{\parallel} / \tan \theta$ are not filtered out.

2.1 Ion half step

- (i) Firstly, calculate the electron velocity at the half step

$$v_{\parallel q}^{n+1/2} = v_{\parallel q}^n + (\Delta t/2)e \nabla_{\parallel} \varphi^{n+1/2}(\mathbf{x}_q^{n+1/2}) .$$

Then the velocity moment $n^{n+1/2} v_{\parallel e}^{n+1/2}$ and density $n^{n+1/2}$ can be calculated using Eqs. (9) and (10).

- (ii) Advance the vorticity, ion parallel velocity and temperature one half step. From Eqs. (11)–(13) we write

$$U^{n+1} = U^{n+1/2} + (\Delta t/2)f_1 \left(U^{n+1/2}, \varphi^{n+1/2}, n^{n+1/2} v_{\parallel i}^{n+1/2}, n^{n+1/2} v_{\parallel e}^{n+1/2} \right)$$

$$\varphi^{n+1} = (\nabla_{\perp}^2)^{-1} U^{n+1}$$

$$v_{\parallel i}^{n+1} = v_{\parallel i}^{n+1/2} + (\Delta t/2) f_2(v_{\parallel i}^{n+1/2}, \varphi^{n+1/2}, n^{n+1/2} T_i^{n+1/2})$$

$$T_i^{n+1} = T_i^{n+1/2} + (\Delta t/2) f_3(T_i^{n+1/2}, \varphi^{n+1/2}, v_{\parallel i}^{n+1/2}) .$$

2.2 Ion full step

- (i) Firstly, advance the electron velocity one full step in a time-centered manner.

$$v_{\parallel q}^{n+1} = v_{\parallel q}^n + \Delta t e \nabla_{\parallel} \varphi^{n+1/2}(\mathbf{x}_q^{n+1/2}) .$$

Then, in order to calculate $n^{n+1} v_{\parallel e}^{n+1}$ we need to predict \mathbf{x}_q^{n+1}

$$\mathbf{x}_q^{n+1} = \mathbf{x}_q^{n-1/2} + (3/2)\Delta t \left\{ \mathbf{v}_{\perp q}^{n+1/2} + 0.5(\mathbf{v}_{\parallel q}^{n+1} + \mathbf{v}_{\parallel q}^n) \right\} .$$

- (ii) Advance the vorticity one full timestep

$$U^{n+3/2} = U^{n+1/2} + \Delta t f_1(U^{n+1}, \varphi^{n+1}, n^{n+1} v_{\parallel i}^{n+1}, n^{n+1} v_{\parallel e}^{n+1})$$

$$\varphi^{n+3/2} = (\nabla_{\perp}^2)^{-1} U^{n+3/2} .$$

- (iii) Then in order to calculate n^{n+1} accurately and to advance the electron position we use a two step process:

$$\mathbf{x}_{q,\text{pred}}^{n+3/2} = \mathbf{x}_q^{n-1/2} + 2\Delta t \left\{ \mathbf{v}_{\perp q}^{n+1/2} + 0.5(\mathbf{v}_{\parallel q}^{n+1} + \mathbf{v}_{\parallel q}^n) \right\} .$$

This enables us to evaluate $\mathbf{v}_{\perp q}^{n+3/2}$ and then,

$$\mathbf{x}_{q,\text{corr}}^{n+1} = \mathbf{x}_q^{n+1/2} + (1/2)\Delta t \left\{ \mathbf{v}_{\parallel q}^{n+1} + 0.5(\mathbf{v}_{\perp q}^{n+1/2} + \mathbf{v}_{\perp q}^{n+3/2}) \right\}$$

$$\mathbf{x}_q^{n+3/2} = \mathbf{x}_q^{n+1/2} + \Delta t \left\{ \mathbf{v}_{\parallel q}^{n+1} + 0.5(\mathbf{v}_{\perp q}^{n+1/2} + \mathbf{v}_{\perp q}^{n+3/2}) \right\} .$$

- (iv) Finally, the ion parallel velocity and temperature are advanced one full timestep

$$v_{\parallel i}^{n+3/2} = v_{\parallel i}^{n+1/2} + \Delta t f_2(v_{\parallel i}^{n+1}, \varphi^{n+1}, n^{n+1} T_i^{n+1})$$

$$T_i^{n+3/2} = T_i^{n+1/2} + \Delta t f_3(T_i^{n+1}, \varphi^{n+1}, v_{\parallel i}^{n+1}) .$$

3. Verification of the Algorithm

3.1 The fluctuating energy k spectrum

The principal tests on the code have involved verifying properties of the real and imaginary frequencies of the linear normal modes, and elucidating the fluctuation spectrum. A test-current analysis of the linearized equations is shown in Appendix A. The resulting dispersion relation is

$$\begin{aligned} \varepsilon(k, \omega) = & \left\{ k^2 \rho_s^2 \left(1 - \frac{\omega_{*i}}{\omega} (1 + \eta_i) \right) \right. \\ & - \frac{k_{\parallel}^2 c_s^2}{\omega^2 - \frac{2}{3} k_{\parallel}^2 c_s^2 / \tau} \left(1 - \frac{\omega_{*i}}{\omega} \eta_i + \frac{1}{\tau} \left(1 + \frac{\omega - \omega_{*e}}{\sqrt{2} k_{\parallel} v_e} Z \right) \right) \\ & \left. + \left(1 - \frac{\omega_{*e}}{\omega} \right) \left(1 + \frac{\omega}{\sqrt{2} k_{\parallel} v_e} Z \right) \right\}. \end{aligned} \quad (14)$$

where Z is the Plasma Dispersion Function [23]. The dispersion relation equation $\varepsilon(k, \omega) = 0$, then determines the linear normal modes of the system.

The fluctuation energy k spectrum is also calculated in Appendix A. The contribution from the high frequency root $\omega_k = \pm \theta \sqrt{\Omega_e \Omega_i}$ in the long wavelength limit $|k_{\perp} \rho_s| \ll 1$ is shown to be

$$W(k) = \frac{1}{2} \left(\frac{\Omega_i}{\omega_i} \right)^2 T_e \quad (15)$$

where $\omega_i = \sqrt{4\pi N_0 e^2 / m_i}$, and N_0 is the number density per unit length in the y direction for a one-dimensional calculation. Therefore, the noise is down by a factor $(\Omega_i / \omega_i)^2$ compared with a fully electrostatic simulation that does not assume charge neutrality. This is the same result as obtained by Krommes *et al.* [24] for the gyrokinetic model. For $|k_{\perp} \rho_s| \gg 1$ we obtained

$$W(k) = \frac{1}{2} \left(\frac{\Omega_i}{\omega_i} \right)^2 T_e / (k_{\perp} \rho_s)^2, \quad (16)$$

the k dependence appears to be unique to the hybrid model.

Three test runs were performed using a one-dimensional version of the code ($\partial_y \neq 0$), without the presence of the convective nonlinearities. In the normalized units that were described in Section 2 the common parameters were $\theta = 8.727 \times 10^{-3} (0.5^\circ)$, $\tau = 100.$, $\omega_e \Delta t = 5$, and there were 4000 timesteps. The electrons were loaded with a maxwellian parallel velocity distribution with thermal velocity $v_e = 1.5$. There were 128 gridpoints in the y -direction and 160 simulation particles per gridpoint. For case (a) $m_e/m_i = 1/100$, $B = 10$, that is $(\Omega_i/\omega_i) = 1$; case (b) $m_e/m_i = 1/1600$, $B = 10$, that is $(\Omega_i/\omega_i) = 1/4$; and case (c) $m_e/m_i = 1/100$, $B = 1$, that is $(\Omega_i/\omega_i) = 1/10$. Figure 2 shows the log plots of the normalized spectrum $W'(k) = W(k)/(T_e/2)$ for cases (a), (b), and (c). For reference, the curves $(\Omega_i/\omega_i)^2/(1 + k_\perp^2 \rho_s^2)$ are plotted along with the numerical points. The correspondence is excellent indicating that the wavenumber dependence is most likely $1/(1 + k_\perp^2 \rho_s^2)$. We tried a number of different analytical methods but were unable to prove this from the model equations; we could only show the correct behavior Eq. (16) in the short wavelength limit. At large values of $k_\perp \rho_s$ the finite particle size effects, and imposed filtering causes the observed discrepancy. Note that for $|k_\perp \rho_s| \ll 1$ the above analysis gives for the spectrum of ion acoustic waves $W(k) = \frac{1}{2}(\Omega_i/\omega_i)^2 T_e (k_\perp \rho_s)^2$ which is smaller than the measured spectrum. For $|k_\perp \rho_s| \gg 1$ the result is $W(k) = \frac{1}{2}(\Omega_i/\omega_i)^2 \theta (k_\perp \rho_s)^3$ which is also relatively small in the range of interest and clearly would be cut off by particle-grid effects and filtering at very high $|k_\perp \rho_s|$. Finally, we note that the case (a), $\Omega_i/\omega_i = 1$, is unphysical in the sense that it violates the quasineutrality assumption. We simply regard this case as a test of the code algorithm against the analytical model.

3.2 Sound wave test

The normal modes of the plasma are solutions of the equation $\epsilon(\omega, k) = 0$. The ion sound wave dispersion relation arises from taking the limit of Z for Boltzmann electrons

$$|\omega/k_{\parallel}v_e| \ll 1.$$

$$Z \approx -\frac{\sqrt{2}\omega}{k_{\parallel}v_e} + i\sqrt{\pi}. \quad (17)$$

With this, and for a homogeneous plasma ($\eta_i = \omega_{*e} = \omega_{*i} = 0$), we get

$$\omega^2 = k_{\parallel}^2 c_s^2 \left(\left(1 + \frac{1}{\tau}\right) / \left(1 + k_{\perp}^2 \rho_s^2\right) \right) + \frac{2}{3} k_{\parallel}^2 v_i^2. \quad (18)$$

The first tests on the code were conducted in the limit $\tau \gg 1$, so that for $k_{\perp}^2 \rho_s^2 \ll 1$ we get the usual result $\omega = \pm k_{\parallel} c_s$.

Once again, a one-dimensional linear version of the code was used. Other relevant parameters are $\theta = 8.727 \times 10^{-3}$ (0.5°), $m_e/m_i = 1/100$, $B = 10$, $\tau = 100$, $\omega_e \Delta t = 20$, for 8000 timesteps. Two cases were considered, where the electrons were initialized with thermal velocities $v_e = 1.5$ and 2.5 . There were 512 gridpoints and 40 simulation particles per gridpoint were used, although good results can be obtained with somewhat fewer than this number. The numerical accuracy of the code is mainly determined by the electron streaming condition $k_{\parallel \max} v_e \Delta t < 1$. This determined the choice of θ , v_e , and Δt ; for the above parameter $k_{\parallel \max} v_e \Delta t = 1.5$ for ($v_e = 2.5$) so for the tests we are operating at the limit of stability. The main reason for pushing this limit is to obtain a long enough time sample in order to resolve the sound wave frequencies. In normalized units we have $c_s = 0.15$ and $\rho_s = 1.5$ (for $v_e = 1.5$); and $c_s = 0.25$ and $\rho_s = 2.5$ (for $v_e = 2.5$).

The dispersion relation of the code algorithm itself is found by evaluating the fluctuation spectrum $W(k, \omega)$ of the homogeneous plasma. Intuitively, it can be seen in Eq. (A14) that this quantity peaks at the zeroes of the dispersion relation. For $c_s = 0.25$, and mode number $m = 15$ ($k_{\perp} = 2\pi m/512 = 0.184$, or $k_{\parallel} = 1.606 \times 10^{-3}$), Figure 3 is a plot of the W as a function of ω , showing distinct peaks close to $\pm k_{\parallel} c_s = \pm 4.02 \times 10^{-4}$. Figure 4 shows the frequency plotted against k_{\parallel} for $c_s = 0.15$ (\bullet), and $c_s = 0.25$ (\times). The solid curves also show the theoretical result obtained from an exact solution of Eq. (14). That the small k_{\parallel} behavior satisfies $\omega \approx \pm k_{\parallel} c_s$ indicates that the kinetic electrons have Boltzmann-like

behavior ($n_e/n_0 = e\varphi/T_e$) in the appropriate regime. The asymptote at high wavenumber can be obtained from the dispersion relation in the limit $|k_\perp \rho_s|^2 \gg 1$; in that case it is $\omega = \pm(k_\parallel/k_\perp)\Omega_i = \pm 8.727 \times 10^{-4}$, and this is clearly shown in Figure 4. We note that this is a pathological limit in the sense that large $|k_\perp \rho_s|$ is inconsistent with the analytical model. Practically speaking, one needs to run with sufficiently many modes so that $k_{\perp\min}\rho_s (= 0.018)$ is much smaller than unity.

3.3 The collisionless drift-wave test

For the second test we reproduced the collisionless drift wave instability (universal mode) in shearless ($k_\parallel/k_\perp = \text{const.}$) geometry. In this case a density gradient inhomogeneity along with finite electron temperature provides the free energy for a growing electrostatic wave with $k_\parallel/k_\perp \ll 1$. The dispersion relation is established theoretically by retaining the ω_{*e} term in Eq. (14), and substituting both the real and imaginary parts of Z where $|\omega/k_\parallel v_e| \ll 1$ from Eq. (17). Then in the limit $\tau \gg 1$,

$$\varepsilon = k_\perp^2 \rho_s^2 - \frac{k_\parallel^2 c_s^2}{\omega^2} + \left(1 - \frac{\omega_{*e}}{\omega}\right) \left(1 + i\sqrt{\frac{\pi}{2}} \frac{\omega}{k_\parallel v_e}\right). \quad (19)$$

Next write $\varepsilon = \varepsilon_1 + i\varepsilon_2$, and the real frequency of the mode is obtained approximately from $\varepsilon_1 = 0$, that is

$$\omega^2(1 + k_\perp^2 \rho_s^2) - \omega\omega_{*e} - k_\parallel^2 c_s^2 = 0. \quad (20)$$

This is the standard form; for example Kadomtsev [25] Eq. (IV.37). There are two solutions which asymptote to the sound wave $\omega = \pm k_\parallel c_s$ for large values of $k_\parallel c_s$. For $|k_\parallel c_s| < \omega_{*e}$ the positive frequency solution is relevant,

$$\omega_k = \omega_{*e}/(1 + k_\perp^2 \rho_s^2). \quad (21)$$

The growth rate for this mode can be approximated from $\gamma = -\varepsilon_2/(\partial\varepsilon_1/\partial\omega)$ for $\omega = \omega_k$; this gives

$$\gamma = \sqrt{\frac{\pi}{2}} \frac{\omega_{*e}^2}{|k_\parallel| v_e} \frac{k_\perp^2 \rho_s^2}{(1 + k_\perp^2 \rho_s^2)^3}, \quad (22)$$

corresponding to the expression derived by Krall and Trivelpiece [26], Eq. (8.16.11).

The collisionless drift wave is implemented in the code using the multiple scale approach of Lee [8]. This amounts to adding a velocity \mathbf{v}_f to the perpendicular electron velocity Eq. (7),

$$\mathbf{v}_f = \frac{c}{B} \hat{\mathbf{b}} \times \nabla \varphi . \quad (23)$$

This velocity accounts for the density gradient in the x -direction, therefore the linear tests may be done using the one-dimensional version of the code. We note also that for two-dimensional runs where the multiple scale approach is used, the boundary conditions on the field and particle velocities can be made periodic in both the x - and y -directions since they represent quantities with the zero order inhomogeneity taken out.

Figure 5(a) shows the real frequency, obtained once again from the fluctuation spectrum as a function of k_\perp . This is done for two different values of $\rho_s/L_n = 0.0175$ (\times), and 0.035 (\bullet). Also, in normalized units $B = 10$, $v_e = 2.5$, $m_e/m_i = 1/100$, $\tau = 100$, $\theta = 8.727 \times 10^{-3}$ (0.5°), $\omega_e \Delta t = 10$, for 8000 timesteps. There were 512 gridpoints in the y -direction and 40 simulation particles per gridpoint. The numerical solutions of the full dispersion relation Eq. (14) are shown also. Note that the trailing off of the values for large k_\perp probably arises from finite particle and filtering effects.

The growth of the mode is manifest as an increasing electrostatic field energy. The growth rate, for $\rho_s/L_n = 0.175$, is shown in Figure 5(b) as a function of θ in degrees of arc. Note that the quantity ρ_s/L_n is increased here so that the instability drives a measurable increase in the electrostatic energy. We also used a smaller timestep, $\omega_e \Delta t = 4$, in order to accurately resolve this growth over 500 timesteps. The peak growth occurs for $\theta \approx 0.5^\circ$. An estimate for the value can be obtained from the electron-wave resonance condition $\omega_{*e}/k_\parallel v_e = 1$; from this we get the condition $(k_\parallel/k_\perp) = (\rho_s/L_n) \sqrt{m_e/m_i}$, or $\theta \approx 1^\circ$. Once again the theoretical result from the dispersion relation is shown. The main significance of this test is that the kinetic wave-particle resonance in the universal mode is well represented by the code.

3.4 The η_i -mode

We now consider the situation where both density and temperature gradients are present in the system. We define $\eta_i = L_n/L_T$ as a measure of the relative magnitude of the temperature gradient drive compared with the density gradient. Once again take the approximation $|\omega/k_{\parallel}v_e| \ll 1$ for the electrons, then the dispersion relation (14) becomes

$$\varepsilon = k_{\perp}^2 \rho_s^2 \left(1 - \frac{\omega_{*i}(1 + \eta_i)}{\omega} \right) - \frac{k_{\parallel}^2 c_s^2}{\omega^2 - \frac{2}{3} k_{\parallel}^2 c_s^2 / \tau} \left(1 + \frac{1}{\tau} - \frac{\omega_{*i}\eta_i}{\omega} \right) + 1 - \frac{\omega_{*e}}{\omega}. \quad (24)$$

This can be solved analytically in several extreme regimes. For $k_{\perp}^2 \rho_s^2 \ll 1$, $|\omega_{*i}\eta_i| > |\omega|$, and $|\omega| > |\omega_{*e}|$, which we can regard as the $\eta_i \gg 1$ regime, the solution is $\omega^3 = -k_{\parallel}^2 c_s^2 \omega_{*i}\eta_i + (2/3)k_{\parallel}^2 v_i^2 \omega$. Neglecting the second term for $\tau \gg 1$ we have the same result as discussed by Kadomtsev [27]

$$\omega = (-k_{\parallel}^2 c_s^2 \omega_{*i}\eta_i)^{1/3}. \quad (25)$$

In our geometry $\omega_{*i} < 0$ so that the pole with the positive growth rate is $\omega = (-1 + i\sqrt{3})/2 |k_{\parallel} c_s|^{2/3} |\omega_{*i}\eta_i|^{1/3}$. For the case where $|\omega| < |\omega_{*e}|$, or $\eta_i \lesssim 1$ the solution is

$$\omega = k_{\parallel} c_s \left(\left(\frac{2}{3} - \eta_i \right) / \tau \right)^{1/2}. \quad (26)$$

This root will have a growing part for $\eta_i > \eta_{\text{crit}} = 2/3$. When $|\omega_{*i}\eta_i| < |\omega|$ the situation reverts back to that which was described in the previous section. Thus, when $|\omega_{*e}| \ll |k_{\parallel} c_s|$ there are three roots $\omega = 0, \pm k_{\parallel} c_s$, the latter corresponding to the sound wave. When $|\omega_{*e}| > |k_{\parallel} c_s|$ the positive branch ($k_{\parallel} c_s$) turns into the unstable branch of the universal drift mode.

Next consider the case of finite $|k_{\perp} \rho_s|^2$. The important new contribution comes from the term $k_{\perp}^2 \rho_s^2 \omega_{*i}(1 + \eta_i)/\omega$ which is traceable back to the term $\mathbf{v}_{Di} \cdot \nabla$ in the polarization drift (due to the inclusion of finite ion mass) in Eq. (1). When $|k_{\perp} \rho_s|$ is greater than unity the solution to Eq. (24) is $\omega = \pm(k_{\parallel}/k_{\perp})\Omega_i$, so the η_i -mode instability is shut off and the same

unphysical asymptote is reached as for the ion sound wave. An approximation for when the above term becomes important, and thus the largest growth rate is [17]

$$k_{\perp} \rho_s \approx 1/\sqrt{1 + \eta_i} . \quad (27)$$

The value of k_{\parallel}/k_{\perp} for the highest growth rate may be estimated by considering when the sound wave frequency approaches the solution (25); thus

$$k_{\parallel}/k_{\perp} = \eta_i \rho_s / L_n . \quad (28)$$

This is somewhat larger than the value $(\rho_s/L_n)\sqrt{m_e/m_i}$ for the universal drift mode, and is indicative of the diminished role that electron-wave resonance plays in the η_i -mode. For typical parameters $\rho_s/L_n = 0.175$, $\eta_i = 2.$, $\rho_s = 2.5$, $m_e/m_i = 1/100$, and $\tau = 1.$, this estimate gives $\theta = 0.35$ (20°), whereas the optimum angle found from an exact solution of the dispersion relation is $\theta = 0.105$ (6°). Combining Eqs. (25), (27) and (28) the largest growth rate can be estimated

$$\gamma \sim \frac{\sqrt{3}}{2} (c_s/L_n) \sqrt{\eta_i + 1} . \quad (29)$$

This turns out to be about five times too large for the values quoted.

We note here that close to the critical η_i , the value of $k_{\perp} \rho_s$, Eq. (27), becomes large. This is once again a regime where the analytical model breaks down; a full treatment needs to accurately include the finite Larmor radius of the ions as with the gyrokinetic model [8]. Therefore, the test cases near marginal stability are once again considered to be tests against the analytical model. Our code may be used to study the η_i -mode away from the marginal case. This is, in effect, a kinetic electron model that parallels the analytical work done by Lee and Diamond [28], where they assumed a Boltzmann electron model.

The real frequency part of the dispersion relation was tested in the same way as in the previous sections, using the fluctuation spectrum. A long time sample is needed in order to

pick up the real frequency, so we took $\eta_i = 2.0$, that is, close to marginal stability. The other parameters were $\rho_s/L_n = 0.011$, $B = 10$, $v_e = 1.5$, $\theta = 8.727 \times 10^{-3}$ (0.5°), $m_e/m_i = 1/100$, $\tau = 1$, $\omega_e \Delta t = 3.0$, for 8000 timesteps. We ran the linear one-dimensional version of the code with 512 gridpoints in the y -direction, and 40 simulation particles per gridpoint. Figure 6(a) shows the plot of ω_r versus k_\perp . The two solid curves show the roots (refer to Fig. 9(a)) with negative real frequency. Superimposed on these waves are the points obtained from the fluctuation spectra, showing significant discrepancy at high k_\perp due to finite particle size effects and filtering. Figure 6(b) shows the growth rate versus k_\perp for $\rho_s/L_n = 0.175$, $\eta_i = 16$, $B = 10$, $v_e = 2.5$, $\theta = 0.105$ (6°), $m_e/m_i = 1/100$, $\tau = 1$, $\omega_e \Delta t = 0.25$ and 2000 timesteps. The curve is obtained from the exact solution of the dispersion relation, while the points are obtained by running the one-dimensional code. It was necessary to impose an initial perturbation on the parallel ion velocity ($\approx 0.1v_i$) in order to observe this instability. This was done at the various values of k_\perp for which the points are shown in the figure. Note that here we have carried out a test of the linear model. We have not done extensive work on the modification to the Boltzmann electron model when kinetic effects are included, nor have we studied the nonlinear η_i -mode. However some initial discussion on these issues was presented in Ref. [29].

4. Nonlinear Collisionless Drift Waves

We have made a number of nonlinear runs for the collisionless drift wave. The $\mathbf{E} \times \mathbf{B}$ nonlinearities that are present in Eqs. (11), (12), and (13) are included. These terms are coded in space centered finite difference form. This technique causes a slow nonlinear instability to develop; to quell this, an artificial viscosity term $\nu \nabla_\perp^2 F$ is added to the right-hand side each of the three equations, where F is U , $v_{\parallel i}$ and T_i respectively. For the runs that we will present here, $\nu = 10^{-3}$ in normalized units in chosen small so as not to substantially alter the results for the important wavenumbers in the problem. We have also coded the nonlinearities

in upwind difference form [30], as discussed in Appendix B. The results are unchanged; this weak dependence on dissipation in the problem is due to the fact that relatively few low k_{\perp} -modes are being excited. For the results presented here the parallel nonlinearities have been left out, although we have found their inclusion to not alter the results significantly.

For the purpose of comparison we first show the results obtained from a code that treats the ions as full dynamic particles, and the electrons as drift kinetic particles [10]. That is, this differs from the hybrid model in the treatment of the ions. Also, the density gradient is treated self-consistently, whereas in the present code the multiple scale approach is used; refer to Section 3.3. The parameters of the run were: $B = 10$, $v_e = 2.5$, $\theta = 8.727 \times 10^{-3}$ (0.5°), $m_e/m_i = 1/100$, $\rho_s/L_n = 0.175$, $\omega_e \Delta t = 4$, for 1000 timesteps, the number of gridpoints in the (x, y) -plane $(N_x, N_y) = (64, 32)$, and the simulation particles were initially uniformly distributed in a grid on the (x, y) -plane $(NP_x, NP_y) = (512, 64)$. Figure 7(a) shows the time history of $\langle E^2/4\pi n kT \rangle$, the volume averaged electrostatic energy. The linear growth phase is clearly seen, and this corresponds to the point in Fig. 5(b) where $\theta = 8.727 \times 10^{-3}$ (0.5°); at $\omega_e t = 1600$ the mode starts to saturate. Figure 7(b) shows the density profile at $\omega_e t = 0$ and 4000. The instability modifies the profile; crudely, it can be seen that $\tilde{n}/n \approx 0.25$, and this compares with the mixing length estimate $1/k_{\perp} L_n = 0.35$. Figure 7(c) shows a three-dimensional plot of the mode amplitude $|\varphi(k_x, k_y)|$ at $\omega_e t = 4000$, and (d) shows a corresponding contour plot of $\varphi(x, y)$. The most obvious structure occurs at $(\ell, m) \equiv (1, 0)$, where $k_x = 2\pi\ell/N_x$ and $k_y = 2\pi m/N_y$.

Figure 8 shows the electrostatic energy for the hybrid model where the $\mathbf{E} \times \mathbf{B}$ ion nonlinearities in the fluid equations are included (a), and where they are left out (b); the parameters for the runs are same as for that described in Figure 7. The first graph corresponds to the run shown in Fig. 7 for the full dynamics model. The linear growth rate appears to be only slightly higher, and the final saturation energy level is the same within a factor of two. It is not clear whether the differences lie in the use of the fluid ion approach, or in the use

of the multiple scale method for the density gradient. The saturation level for the case of linear ions is about five times higher, and this would appear to be significant since the runs are otherwise identical in the hybrid model. Figure 8(c) and (d) show the electron density as a function of x with and without the ion nonlinearities, respectively. This is shown for times $\omega_e t = 0$ and $\omega_e t = 4000$. Note that the density gradient has been separated out of the problem as an external drive (multiple scale), so the initial profile is flat. For case (c), $\tilde{n}/n \approx 0.37$, and this compares with the mixing length estimate $1/k_\perp L_n = 0.35$. Note that this indicates that the same saturation mechanism via profile modification is acting here as in the case of the full dynamics treatment. Figure 8(e) and (f) show respective plots of $|\varphi(k_x, k_y)|$ also at $\omega_e t = 4000$. The important difference is that when the ion nonlinearities are absent the dominant amplitude occurs where the linear growth is strongest; namely for $(\ell, m) = (0, 1), (1, 1)$, and $(1, -1)$. However, in the nonlinear case (e) there is a dominant mode at $(1, 0)$, and this is the same mode that was present in the full dynamics description. This structure is primarily associated with the vorticity equation (11), and has been discussed in related work [31]. The nonlinear term proportional to $\mathbf{k}_1 \times \mathbf{k}_2 \cdot \hat{\mathbf{b}}$ tends to ‘rotate’ the spectrum in the (k_x, k_y) plane as we have found. Figure 8(g) and (h) show the respective contour plots of $\varphi(x, y)$ at the same time. It can be clearly seen how in the linear case the dominant mode has $k_x = 0$, but for the nonlinear case there is a predominance of $k_y = 0$, that is $(1, 0)$. A number of other runs have been performed with the $\mathbf{E} \times \mathbf{B}$ nonlinearity removed from the electron dynamics; these are basically one-dimensional runs. Details have been presented elsewhere by the present authors [32], and we note the work of Horton [33] who has presented theoretical arguments for the importance of this nonlinearity as a saturation mechanism. In our case it was found that with or without the ion nonlinearities these runs failed to saturate. The electrostatic energy $\langle E^2/4\pi nT \rangle$ grew to unity and thereafter the parallel electron distribution function $f(v_\parallel)$ become grossly distorted. The runs either became excessively noisy, or they were halted when particles moved out of the physical domain.

5. Conclusions

We have developed and tested a new computer algorithm for the study of low-frequency plasma instabilities. The electric potential is obtained from the vorticity equation (11), as is done for the reduced magnetohydrodynamics model [13, 16]. Here the important physics comes from the perpendicular polarization drift, due to the finite mass of the ions; through the continuity equation, quasineutrality is maintained by balancing this drift with the parallel motion of both ions and electrons. The new features are that the parallel electron motion is treated kinetically (i.e., not adiabatically) so that wave-particle resonance effects, and the electron nonlinearity are included. The code was tested for ion sound wave propagation, and it gave the correct linearized η_i -mode dispersion properties. These are important tests for the fluid-ion and Boltzmann-electron properties in regimes where they should apply. We also tested for the collisionless drift wave dispersion properties; here the kinetic properties of the electrons play an important role. The long-wavelength fluctuation spectrum is proportional to $\frac{1}{2} (\Omega_i/\omega_i)^2 T_e$ per mode, where the factor $(\Omega_i/\omega_i)^2$ indicates the low-noise character of the algorithm. This is the same as the result obtained by Krommes *et al.* [24] for the gyrokinetic model. We note our use of the vorticity equation to obtain the electrostatic potential in terms of the parallel derivative of the current, whereas in conventional electrostatic codes the potential is obtained from poisson's equation. The measured fluctuation spectrum of the code does not exceed the theoretical estimate; only at high wavenumber k is there some discrepancy due to the particle-grid effects.

We performed nonlinear test runs in the collisionless drift wave regime. When the $\mathbf{E} \times \mathbf{B}$ nonlinearities are included in the three equations (11)–(13), the saturation level density fluctuations obeys the mixing length estimate $\tilde{n}/n_0 \approx 1/k_\perp L_n$. This result was also checked against an identical run done with a code that treats the ions with full dynamics. We note that the term proportional to $\mathbf{k}_1 \times \mathbf{k}_2 \cdot \hat{\mathbf{b}}$ in the vorticity equation tends to generate finite k_x

(for $k_y = 0$) components of $|\varphi_{\mathbf{k}}|$.

The model can be expanded to include the nonlinearities due to the density perturbation on the left-hand side of Eq. (1). We have already noted in Section 4 that this code may be used to assess the relative importance of the electron and ion nonlinearities [32, 33]. Finally, we are employing the code to study trapped electron modes in sheared geometry [34].

Acknowledgments

We would like to thank B.A. Carreras, P.H. Diamond, R.D. Hazeltine, G.S. Lee, and P.W. Terry for their assistance in this work. Also, one of us (PML) would like to thank R. Dory and the staff at Oak Ridge National Laboratory, Fusion Energy Division, for their hospitality during my stay there. This work was supported by the U.S. Department of Energy under contracts DE-FG05-80ET-53088 with the Institute for Fusion Studies, The University of Texas at Austin, and DE-AC05-84-OR21400 with Martin Marietta Energy Systems, Inc.

Appendix A: Model Dispersion Relation and Fluctuation Spectrum

We calculate the dispersion relation for the linearized model equations, and find expressions for the fluctuation spectrum. We perform a test-current analysis of the linearized equations, similar to the calculation of Krall and Trivelpiece [26]. That is, the response potential $\varphi(\mathbf{x}, t)$ in Eq. (1) is calculated for an electron current $-ev_{\parallel}\delta(\mathbf{x} - \mathbf{x}')$ where $\mathbf{x}' = \mathbf{x}'_0 + \mathbf{v}'_0 t$. Much of the results in this section will pertain to the one-dimensional version of the code, so we perform the analysis retaining only terms with variation in the y -direction. Otherwise the geometry is the same as shown in Fig. 1. The equations will be Fourier transformed in space with the convention $\frac{1}{2\pi} \int dy e^{-iky}$, and Laplace transformed in time according to $\int dt e^{i\omega t}$. The test-current perturbed Eq. (1) is

$$N_0 \rho_s^2 (\partial_t + v_{Di} \cdot \nabla) \nabla_{\perp}^2 \left(\frac{e\varphi}{T_e} \right) - N_0 \nabla_{\parallel} (v_{\parallel i} - v_{\parallel e}) = \nabla_{\parallel} (v_0/\theta) \delta(y - y') \quad (\text{A1})$$

where $v_{\parallel} = v_0/\theta$ ($\theta \ll 1$) and N_0 is the number density per unit length in the y -direction. The Fourier-Laplace transform is performed and, in what follows, the transient response of the plasma is ignored.

$$N_0 \rho_s^2 k^2 (-i\omega + i\omega_{*i}(1 + \eta_i)) \left(\frac{e\varphi_k}{T_e} \right) + N_0 i k_{\parallel} (v_{\parallel i} - v_{\parallel e}) = \frac{k_{\parallel}}{2\pi} \left(\frac{v_0}{\theta} \right) \frac{e^{-iky'_0}}{\omega - kv'_0} \quad (\text{A2})$$

where $\omega_{*i} = -(T_i/T_e)\omega_{*e} = -kcT_i/eBL_n$. The ion response is calculated using Eqs. (2) and (3)

$$v_{\parallel i} = \frac{ek_{\parallel}}{\omega m_i} \varphi_k + \frac{k_{\parallel}}{\omega m_i} T_i^{(1)} + \frac{T_i k_{\parallel}}{\omega m_i n_0} n^{(1)} \quad (\text{A3})$$

$$T_i^{(1)} = -\frac{\omega_{*i}}{\omega} \eta_i T_e \left(\frac{e\varphi_k}{T_e} \right) + \frac{2}{3} T_i \frac{k_{\parallel}}{\omega} v_{\parallel i} . \quad (\text{A4})$$

The equations (6), (7), and (8) for the electrons correspond to a lagrangian solution (or solution by characteristics), of a form of the drift kinetic equation (DKE)

$$\left[\partial_t + \mathbf{v}_{\parallel} \cdot \nabla_{\mathbf{x}} + \frac{c}{B} \hat{\mathbf{b}} \times \nabla \varphi \cdot \nabla_{\mathbf{x}} + \frac{e}{m} \nabla_{\parallel} \varphi \partial_{v_{\parallel}} \right] f_e(\mathbf{x}, v_{\parallel}, t) = 0, \quad (\text{A5})$$

where $f(\mathbf{x}, v_{\parallel}, t)$ is the distribution function. This is appropriate for our model with zero electron Larmor radius, including full dynamics parallel to the magnetic field and $\mathbf{E} \times \mathbf{B}$ drifts in the perpendicular direction. The electron response can be calculated by linearizing the DKE about a maxwellian distribution.

$$f_e = f_0 + f^{(1)}, \quad (\text{A6})$$

where $f_0 = \frac{1}{\sqrt{2\pi}v_e} e^{-v_{\parallel}^2/2v_e^2}$, and v_e is the thermal velocity. We evaluate the perturbed distribution function

$$f^{(1)} = \left(\frac{e\varphi_k}{T_e} \right) \left(1 - \frac{\omega - \omega_{*e}}{\omega - k_{\parallel}v_e} \right) f_0, \quad (\text{A7})$$

and then the perturbed electron density and parallel velocity,

$$n^{(1)} = n_0 \int f^{(1)} dv_{\parallel} = n_0 \left(\frac{e\varphi_k}{T_e} \right) \left(1 + \frac{\omega - \omega_{*e}}{\sqrt{2}|k_{\parallel}|v_e} Z \left(\frac{\omega}{\sqrt{2}|k_{\parallel}|v_e} \right) \right), \quad (\text{A8})$$

$$v_{\parallel e} = \int f^{(1)} v_{\parallel} dv_{\parallel} = \left(\frac{e\varphi_k}{T_e} \right) \frac{\omega - \omega_{*e}}{k_{\parallel}} \left(1 + \frac{\omega}{\sqrt{2}|k_{\parallel}|v_e} Z \left(\frac{\omega}{\sqrt{2}|k_{\parallel}|v_e} \right) \right), \quad (\text{A9})$$

where $Z(\xi) = (1/\sqrt{\pi}) \int_{-\infty}^{\infty} dx e^{-x^2}/(x-\xi)$ is the Plasma Dispersion Function [23]. Combining Eqs. (A2), (A3), (A4), (A8), and (A9) we arrive at an expression for the perturbed potential

$$\varphi_k(\omega) = \frac{iT_e k v_0' e^{-iky_0'}}{2\pi e N_0 (\omega - k v_0') \varepsilon(k, \omega) \omega}, \quad (\text{A10})$$

where

$$\begin{aligned} \varepsilon(k, \omega) = & \left\{ k^2 \rho_s^2 \left(1 - \frac{\omega_{*i}}{\omega} (1 + \eta_i) \right) \right. \\ & - \frac{k_{\parallel}^2 c_s^2}{\omega^2 - \frac{2}{3} k_{\parallel}^2 c_s^2 / \tau} \left(1 - \frac{\omega_{*i}}{\omega} \eta_i + \frac{1}{\tau} \left(1 + \frac{\omega - \omega_{*e}}{\sqrt{2}|k_{\parallel}|v_e} Z \right) \right) \\ & \left. + \left(1 - \frac{\omega_{*e}}{\omega} \right) \left(1 + \frac{\omega}{\sqrt{2}|k_{\parallel}|v_e} Z \right) \right\}. \end{aligned} \quad (\text{A11})$$

The dispersion relation $\varepsilon(k, \omega)$ then determines the linear normal modes of the system we are describing.

One important test of a code is to compare the fluctuating energy k spectrum for a homogeneous stable plasma with the theoretical estimate. We first evaluate the fluctuating energy in terms of the average over the maxwellian distribution of particles

$$\frac{\langle E^2(y) \rangle}{8\pi} = \frac{N_0}{8\pi} \int dy' \int dv'_{\parallel} f_0(v'_{\parallel}) E(y, y', v'_{\parallel}) E^*(y, y', v'_{\parallel}) , \quad (\text{A12})$$

where the electric field due to the test current is

$$E(y, y', v'_{\parallel}) = \int \frac{dk}{2\pi} \frac{iT_e k e^{ik(y-y')}}{eN_0 \varepsilon(k, kv'_0)} . \quad (\text{A13})$$

Then, defining

$$\frac{\langle E^2(y) \rangle}{8\pi} = \int \frac{dk}{2\pi} W(k),$$

we obtain the fluctuating energy spectral density

$$W(k) = \frac{T_e^2}{8\pi N_0 \theta e^2} \int_{-\infty}^{\infty} d\omega f_0 \left(\frac{\omega}{k_{\parallel}} \right) \frac{k}{|\varepsilon(k, \omega)|^2} . \quad (\text{A14})$$

A closed form for the frequency integral could not be obtained, however, we can estimate the result by taking the high frequency approximation of the dispersion relation. In the limit $|\omega/\sqrt{2} k_{\parallel} v_e| \gg 1$

$$Z \approx -\frac{\sqrt{2} k_{\parallel} v_e}{\omega} - \sqrt{2} \left(\frac{k_{\parallel} v_e}{\omega} \right)^3 + i\sqrt{\pi} \exp \left[-(\omega/\sqrt{2} k_{\parallel} v_e)^2 \right] , \quad (\text{A15})$$

and writing

$$\varepsilon(k, \omega) = \varepsilon_1 + i\varepsilon_2$$

we have

$$\begin{aligned} \varepsilon_1 &= k^2 \rho_s^2 \left(1 - \frac{\theta^2 \Omega_e \Omega_i}{\omega^2} \right) \\ \varepsilon_2 &= \sqrt{\frac{\pi}{2}} \frac{\omega}{|k_{\parallel}| v_e} \exp \left[-(\omega/\sqrt{2} k_{\parallel} v_e)^2 \right] . \end{aligned} \quad (\text{A16})$$

The high frequency root is approximately given by $\omega_k = \pm\theta\sqrt{\Omega_e\Omega_i}$. The contribution to the argument of Eq. (A14) can be estimated by expanding ε about ω_k [35].

$$\text{Im } \frac{1}{\varepsilon} \approx \frac{\pi}{\frac{\partial \varepsilon_1}{\partial \omega_k}} \left[\delta \left(\omega + \theta\sqrt{\Omega_e\Omega_i} \right) + \delta \left(\omega - \theta\sqrt{\Omega_e\Omega_i} \right) \right] . \quad (\text{A17})$$

With this, the integral Eq. (32) can be performed

$$W(k) = \frac{1}{2} \left(\frac{\Omega_i}{\omega_i} \right)^2 T_e \quad (\text{A18})$$

where $\omega_i = \sqrt{4\pi N_0 e^2 / m_i}$. For a fully electrostatic code that solves Poisson's equation $\nabla^2 \varphi = -4\pi \rho$, where ρ is the charge density, the low k spectral density ($k\lambda_D \ll 1$) is equal to $(1/2)T_e$. Thus, the use of the quasineutral hybrid model in the present study gives rise to a further noise reduction factor $(\Omega_i/\omega_i)^2$. This is the same result as obtained by Krommes *et al.* [24] for the gyrokinetic model. For $|k_\perp \rho_s| \gg 1$ we have $\varepsilon(k, \omega) \rightarrow k_\perp^2 \rho_s^2$ and in that limit Eq. (A14) gives $W(k) = \frac{1}{2} (\Omega_i/\omega_i)^2 T_e / (k_\perp \rho_s)^2$.

Appendix B: Treatment of the Nonlinear Terms

The upwind differencing of the convective nonlinearities is discussed in reference [30]. In our case we used a variation obtained in private communication with K.E. Torrance of Cornell University. This is a conservative form, which is called conserving upwind differencing or the “second upwind method”. The relevant $\mathbf{E} \times \mathbf{B}$ nonlinearities in Eqs. (11), (12), and (13) can be written in the general conservative form,

$$\partial_t f = -\nabla \cdot \mathbf{u} f + \dots, \quad (\text{B1})$$

where $\mathbf{u} = \hat{\mathbf{b}} \times \nabla \varphi$. In the approximation $|k_{\parallel}/k_{\perp}| \ll 1$, the finite difference form for the right-hand side is expressed

$$\partial_t f_{ij} = -\delta_x^*(uf) - \delta_y^*(vf) \quad (\text{B2})$$

where (i, j) refers to (x, y) gridpoint position, and

$$\begin{aligned} \delta_x^*(uf) = \frac{1}{2\Delta x} & \left\{ \left(u_{i+\frac{1}{2}} - |u_{i+\frac{1}{2}}| \right) T_{i+1} \right. \\ & \left. + \left(u_{i+\frac{1}{2}} + |u_{i+\frac{1}{2}}| - u_{i-\frac{1}{2}} + |u_{i-\frac{1}{2}}| \right) T_i - \left(u_{i-\frac{1}{2}} + |u_{i-\frac{1}{2}}| \right) T_{i-1} \right\} \end{aligned} \quad (\text{B3})$$

$$\begin{aligned} \delta_y^*(vf) = \frac{1}{2\Delta y} & \left\{ \left(v_{j+\frac{1}{2}} - |v_{j+\frac{1}{2}}| \right) T_{j+1} + \left(v_{j+\frac{1}{2}} + |v_{j+\frac{1}{2}}| - v_{j-\frac{1}{2}} + |v_{j-\frac{1}{2}}| \right) T_j \right. \\ & \left. - \left(v_{j-\frac{1}{2}} + |v_{j-\frac{1}{2}}| \right) T_{j-1} \right\}, \end{aligned} \quad (\text{B4})$$

and where in our normalized units $\Delta x = \Delta y = \Delta$. These expressions have the advantage of not having to use Fortran IF statements in their coding. The face centered transport velocities are evaluated as

$$u_{i+\frac{1}{2}} = -\partial_y \varphi \Big|_{i+\frac{1}{2}} = \frac{1}{4\Delta y} (-\varphi_{i,j+1} - \varphi_{i+1,j+1} + \varphi_{i,j-1} + \varphi_{i+1,j-1}),$$

$$\begin{aligned}
u_{i-\frac{1}{2}} &= -\partial_y \varphi \Big|_{i-\frac{1}{2}} = \frac{1}{4\Delta y} (-\varphi_{i,j+1} - \varphi_{i-1,j+1} + \varphi_{i,j-1} + \varphi_{i-1,j-1}) , \\
v_{j+\frac{1}{2}} &= \partial_x \varphi \Big|_{j+\frac{1}{2}} = \frac{1}{4\Delta x} (\varphi_{i+1,j} + \varphi_{i+1,j+1} - \varphi_{i-1,j} - \varphi_{i-1,j+1}) , \\
v_{j-\frac{1}{2}} &= \partial_x \varphi \Big|_{j-\frac{1}{2}} = \frac{1}{4\Delta x} (\varphi_{i+1,j} + \varphi_{i+1,j-1} - \varphi_{i-1,j} - \varphi_{i-1,j-1}) ,
\end{aligned} \tag{B5}$$

This treatment of the convection is only first order accurate in space, $\mathcal{O}[\Delta x, \Delta y]$. It has the advantage that for numerical stability there are no formal mesh size restrictions. It does introduce artificial viscosity, however in our application only the low order modes of the (k_x, k_y) spectrum are excited, so no serious errors arise. Under conditions where many modes are excited, one should use grid refinement, or higher order techniques to check the numerical accuracy.

References

1. J.A. Byers, B.I. Cohen, W.C. Condit, and J.D. Hanson, J. Comput. Phys., **27**, 363 (1978).
2. C.G. Darwin, Phil. Mag., **39**, 537 (1920).
3. D.W. Hewett, J. Comput. Phys. **38**, 378 (1980).
4. D.S. Harned, J. Comput. Phys. **47**, 452 (1982).
5. A. Mankofsky, R.N. Sudan, and J. Denavit, J. Comput. Phys. **70**, 89 (1987).
6. D.W. Hewett and C.W. Nielson, J. Comput. Phys. **29**, 219 (1978).
7. in *Multiple Timescales*, edited by J.U. Brackbill and B.I. Cohen (Academic, Orlando, 1985).
8. W.W. Lee, J. Comput. Phys. **72**, 243 (1987).
9. H. Okuda, Space Science Reviews **47**, 41 (1985).
10. W.W. Lee and H. Okuda, J. Comput. Phys. **26**, 139 (1978).
11. D.A. D'Ippolito and R.C. Davidson, Phys. Fluids **18**, 1507 (1975).
12. M. Yagi, M. Wakatani, and A. Hasegawa, in Proc. U.S.-Japan Workshop on "Structures in Magnetically Confined Plasmas," Research Report NIFS — PROC Series, ISSN 0915-6348, Nagoya, Japan, March (1989) p. 161.
13. H.R. Strauss, Phys. Fluids **20**, 1354 (1977).
14. W.W. Lee, Y.Y. Kuo, and H. Okuda, Phys. Fluids **21**, 617 (1978).
15. A. Hasegawa, and M. Wakatani, Phys. Fluids **27**, 611, (1984).

16. R.D. Hazeltine, M. Kotschenreuther, and P.J. Morrison, *Phys. Fluids* **28**, 2466 (1985).
17. W. Horton, R.D. Estes, and D. Biskamp, *Plasma Phys.* **22**, 663 (1980).
18. S. Tsai, F.W. Perkins, and T.H. Stix, *Phys. Fluids* **13**, 2108 (1970).
19. F.L. Hinton and C.W. Horton, Jr., *Phys. Fluids* **14**, 116 (1971).
20. C.W. Horton, Jr. and R.K. Varma, *Phys. Fluids* **15**, 620 (1972).
21. S.I. Braginskii, in *Reviews of Plasma Physics*, Ed. M.A. Leontovich (Consultants Bureau, NY, 1965), Vol. I, p. 205.
22. C.K. Birdsall and A.B. Langdon, *Plasma Physics via Computer Simulation* (McGraw-Hill, NY, 1985) p. 240.
23. B.D. Fried and S.D. Conte, *The Plasma Dispersion Function* (Academic, NY, 1961).
24. T.A. Krommes, W.W. Lee, and C. Oberman, *Phys. Fluids* **29**, 2421 (1986).
25. B.B. Kadomtsev, in *Plasma Turbulence* (Academic Press, NY, 1965).
26. N.A. Krall and A.W. Trivelpiece, *Principles of Plasma Physics* (McGraw-Hill, NY, 1973) p. 563.
27. B. Kadomtsev and O.P. Pogutse, in *Reviews of Plasma Physics*, Vol. V, p. 249, (Consultants Bureau, NY, 1970).
28. G.S. Lee and P.H. Diamond, *Phys. Fluids* **29**, 3291 (1986).
29. J.-N. Leboeuf and P.M. Lyster, *Bull. Amer. Phys. Soc.* **33**, 2074 (1988).
30. R. Peyret and T.D. Taylor, *Computational Methods for Fluid Flow*, Springer-Verlag, NY (ISBN 11147-6), (1983), p. 29.

- 31. A. Hasegawa, C. MacLennan, and Y. Kodama, Phys. Fluids **22**, 2122 (1979); H. Okuda, T. Sato, A. Hasegawa, and R. Pellat, Phys. Fluids **23**, 1965 (1980); H. Okuda, Phys. Fluids **23**, 498 (1980); P.W. Terry and W. Horton, Phys. Fluids **26**, 106 (1983); R.E. Waltz, Phys. Fluids **26**, 169 (1983).
- 32. P.M. Lyster and J.-N. Leboeuf, Proc. U.S.-Japan Workshop on “Structures in Confined Plasmas,” Research Report NIFS — PROC Series, ISSN 0915-6348, Nagoya, Japan, March (1989) p. 151.
- 33. W. Horton, Phys. Rev. Lett. **37**, 1269 (1976).
- 34. R.H. Fowler, J.-N. Leboeuf, B.A. Carreras, P.H. Diamond, P.M. Lyster, Bull. Amer. Phys. Soc. **34**, 2046 (1989).
- 35. S. Ichimaru, *Basic Principles of Plasma Physics: A Statistical Approach*, in Frontier in Physics (Benjamin/Cummings, Reading, Massachusetts, 1973) p. 61 and 210.

Figure Captions

1. The schematic sketch of sheared slab configuration.
2. The logarithm of the normalized fluctuation spectrum $W'(k)$ for (a) $\Omega_i/\omega_i = 1$, (b) $\Omega_i/\omega_i = 1/4$, and (c) $\Omega_i/\omega_i = 1/10$.
3. The fluctuation spectrum $W(k, \omega)$ for a homogeneous plasma with $c_s = 0.25$ at $k_{\parallel} = 1.606 \times 10^{-3}$.
4. The sound-wave dispersion relation for $c_s = 0.15$ (\bullet) and 0.25 (\times).
5. (a) Collisionless drift wave real frequency dispersion relation. (b) Collisionless drift wave growth rate.
6. (a) The η_i -mode real frequency dispersion relation. (b) The η_i -mode growth rate.
7. (a) The electrostatic energy, normalized to the total particle energy, for the standard collisionless drift wave using the model containing full ion dynamics. (b) The electron density profile at $\omega_e t = 0$, and 4000. (c) The spectral amplitude $|\varphi(k_x, k_y)|$ at $\omega_e t = 4000$, and (d) the corresponding contours of $\varphi(x, y)$; $\varphi_{\max} = 4.1$, $\varphi_{\min} = -4.1$.
8. The electrostatic energy as a function of time for (a) nonlinear collisionless drift wave using the hybrid model, and (b) the case where the ion equations are linearized. (c) and (d) show the respective electron density profiles at $t = 0$ (flat profile) and $\omega_e t = 4000$. (e) and (f) show the respective plots of spectral amplitude $|\varphi(k_x, k_y)|$ at $\omega_e t = 4000$. (g) shows the contour plot of $\varphi(x, y)$ for nonlinear run, $\varphi_{\max} = 6.5$, $\varphi_{\min} = -6.4$, and (h) shows the contour plot of $\varphi(x, y)$ for the linear run, $\varphi_{\max} = 9.8$, $\varphi_{\min} = -10.7$.

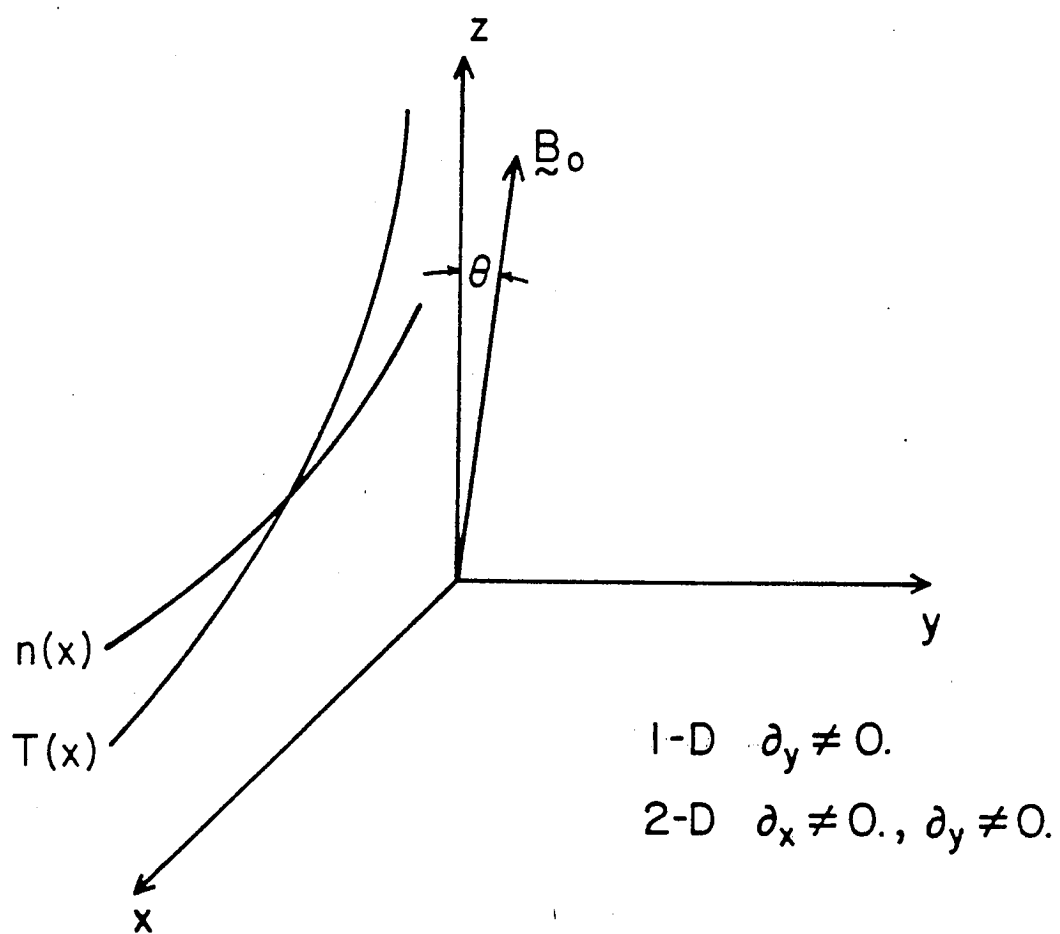


Fig. 1

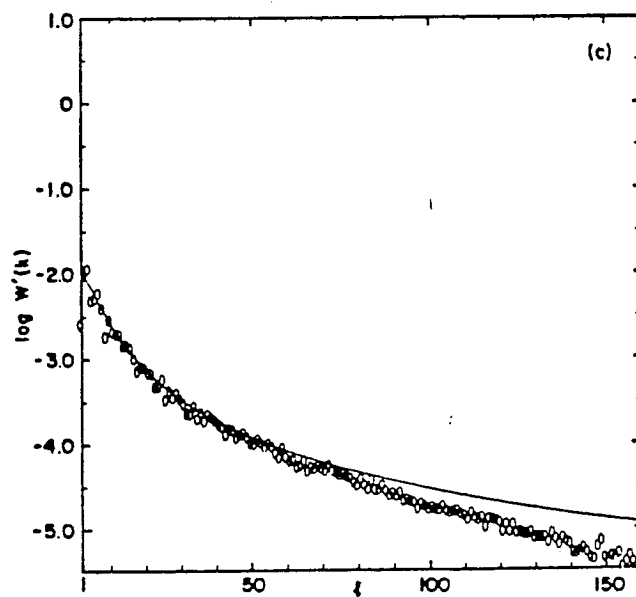
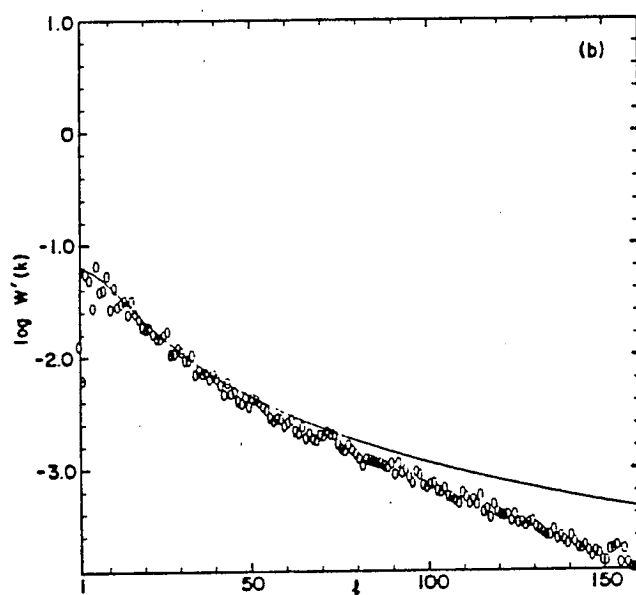
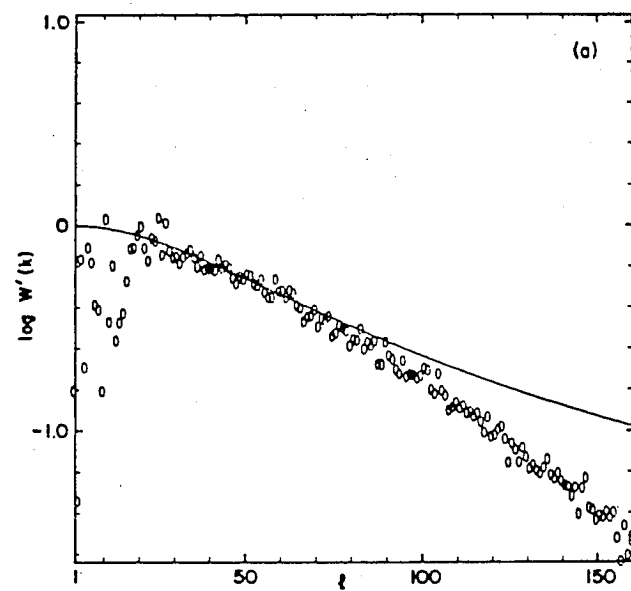


Fig. 2

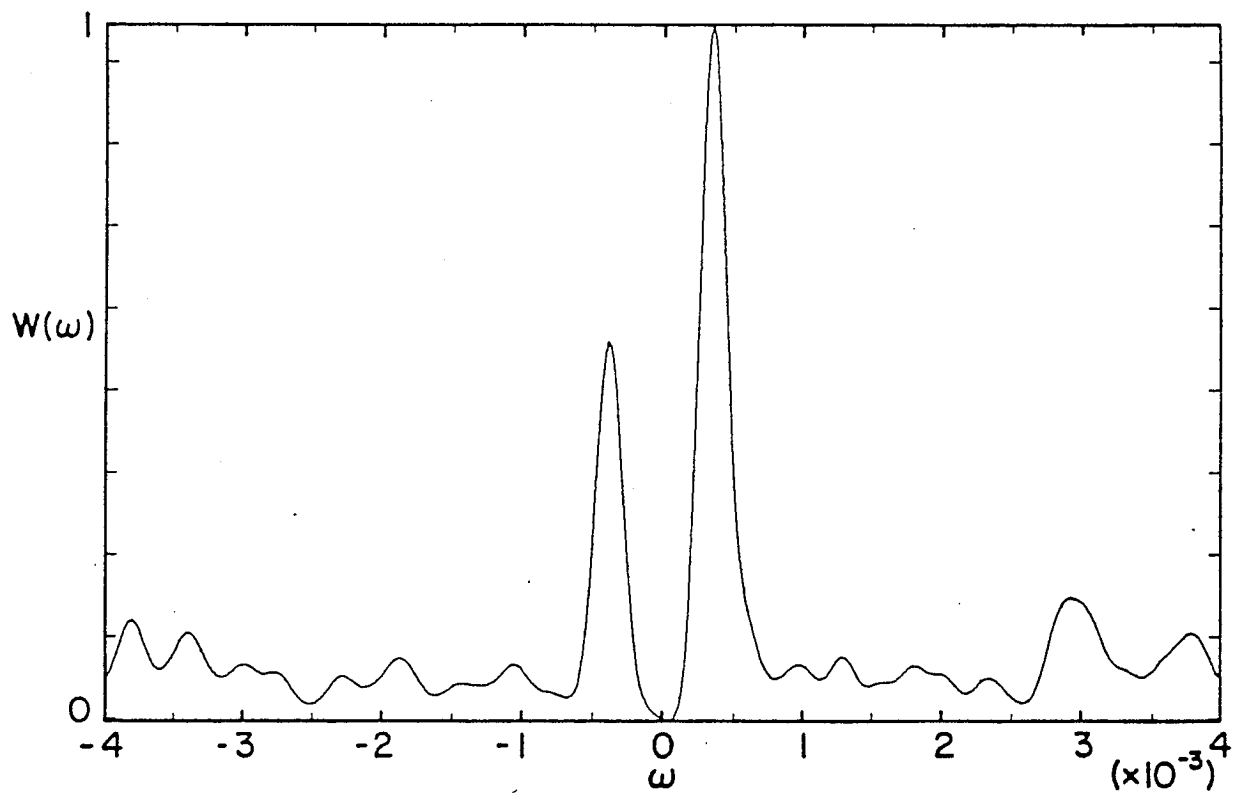


Fig. 3

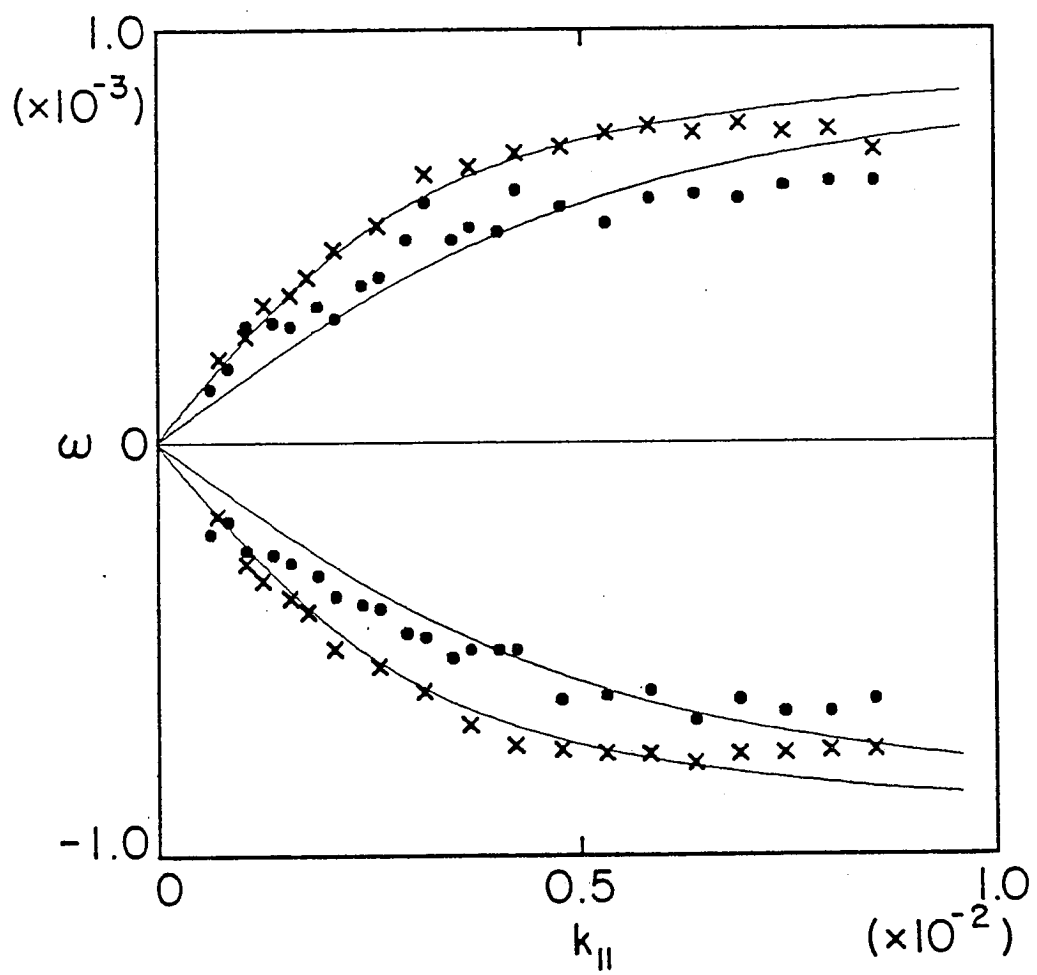


Fig. 4

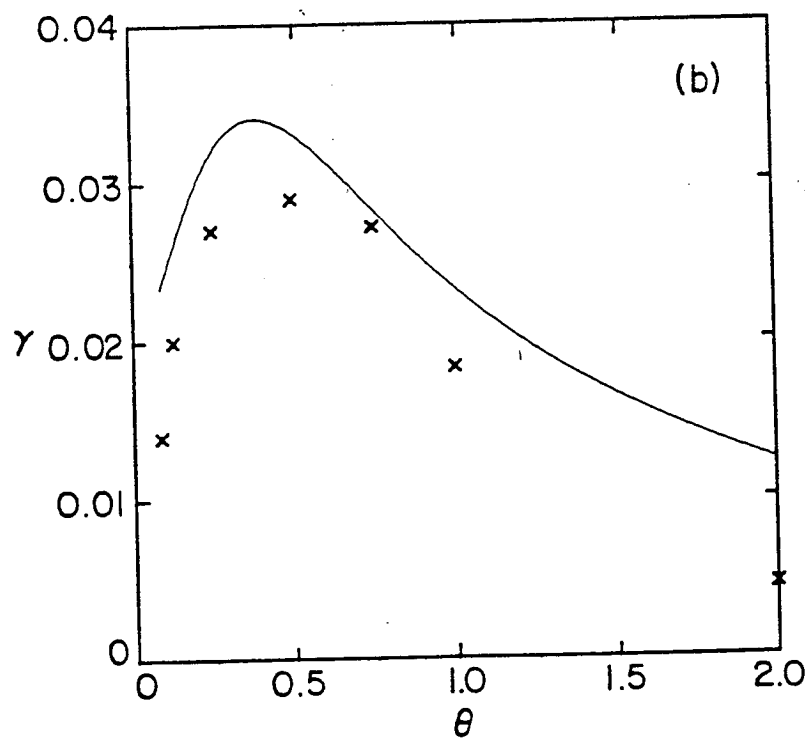
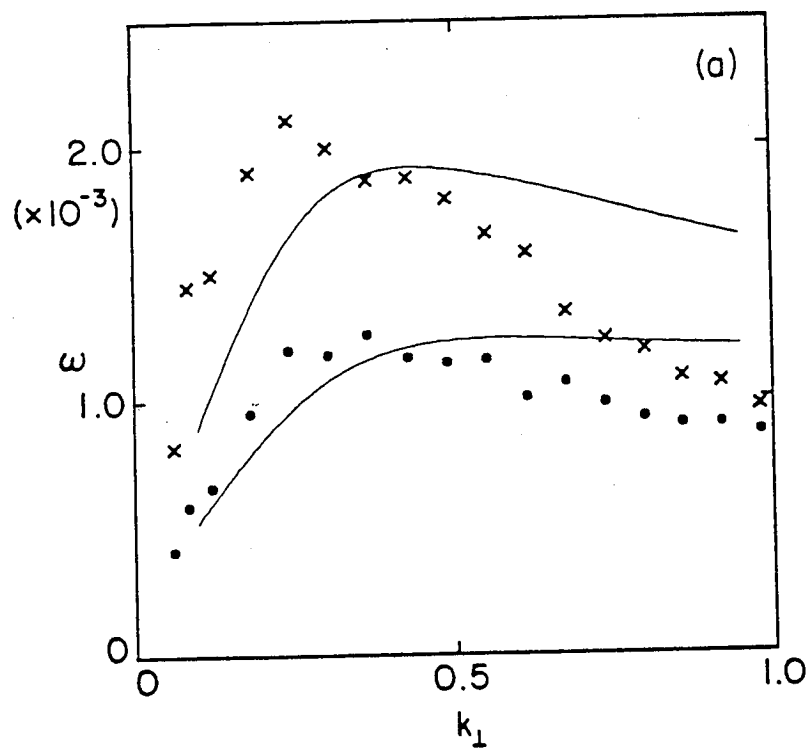


Fig. 5

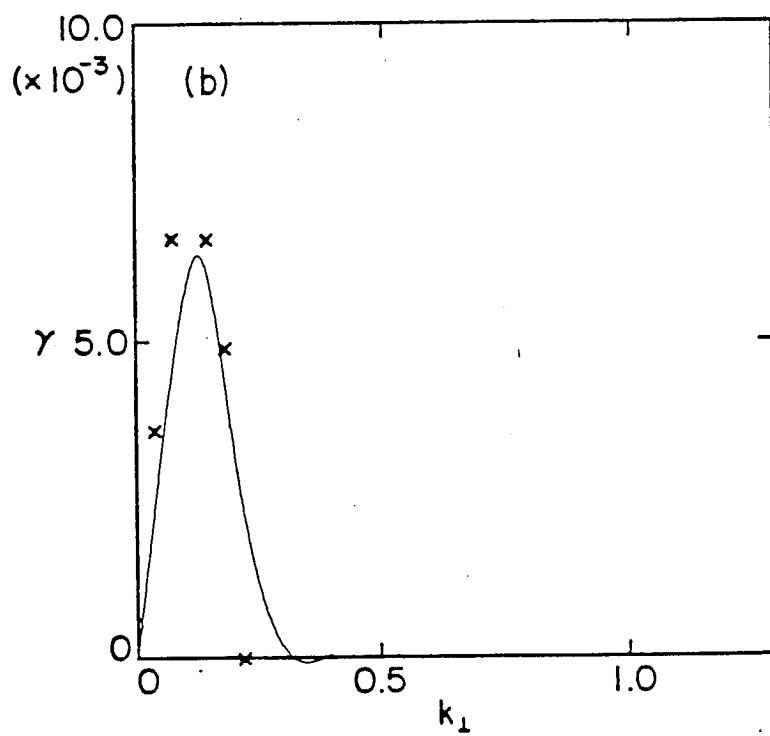
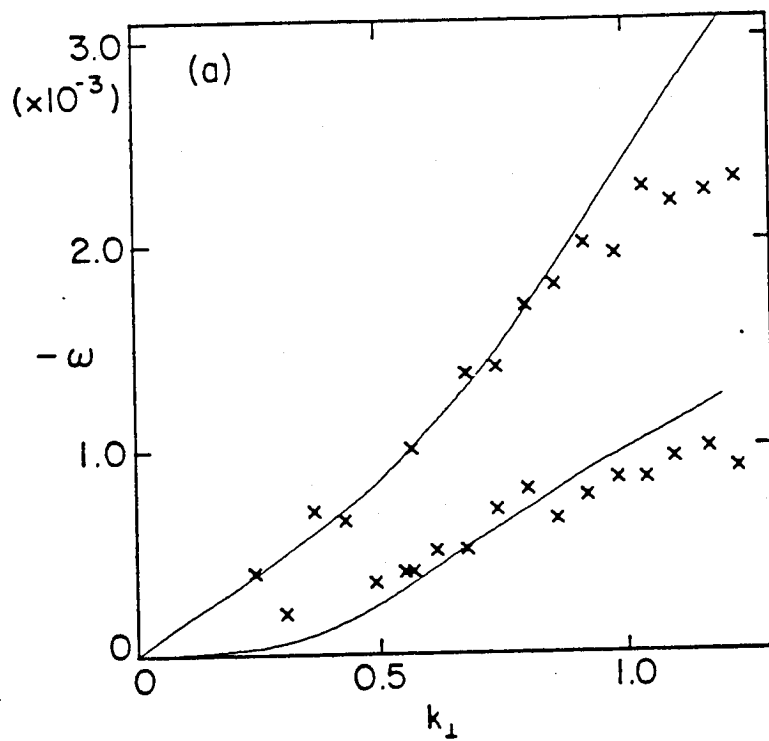


Fig. 6

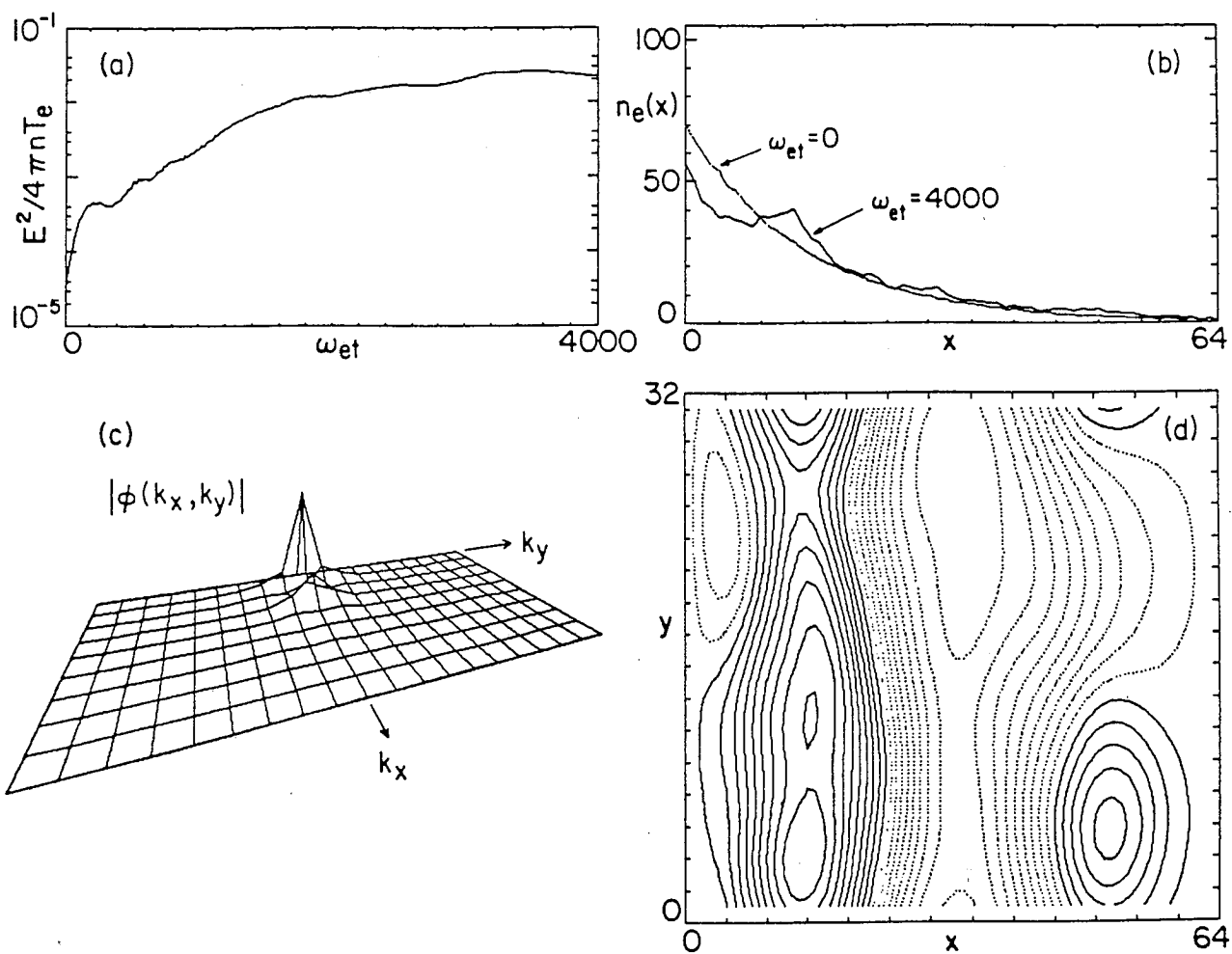


Fig. 7

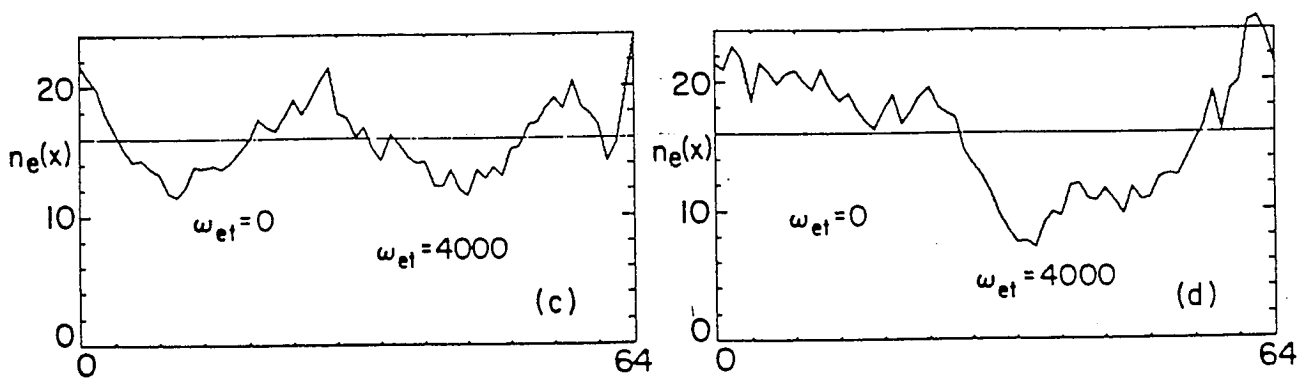
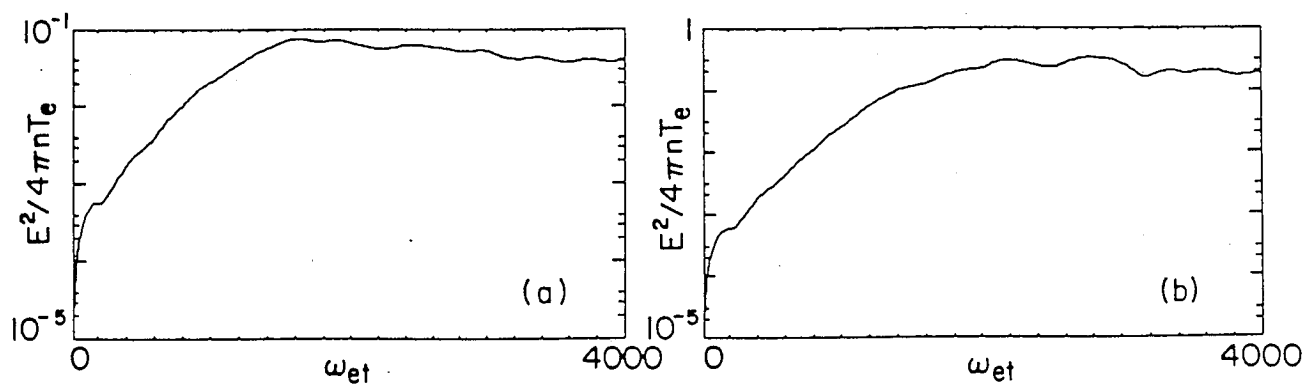


Fig. 8(a)-(d)

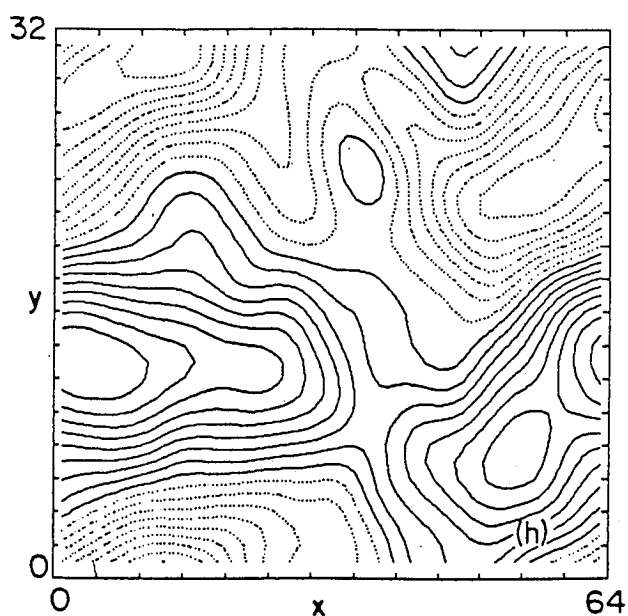
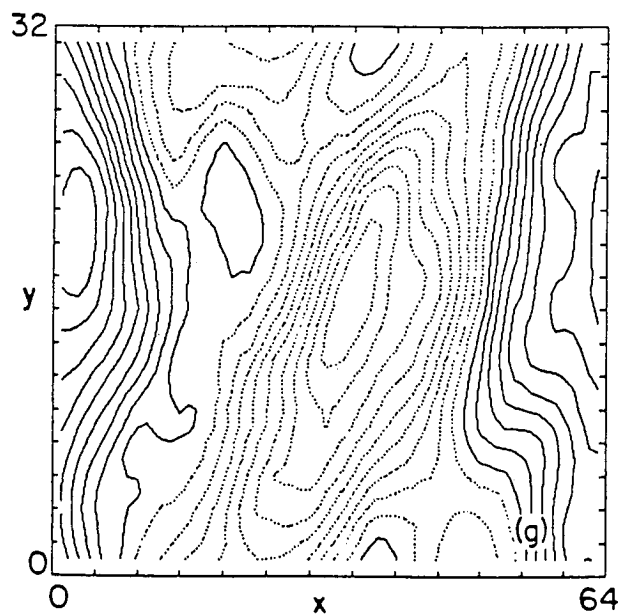
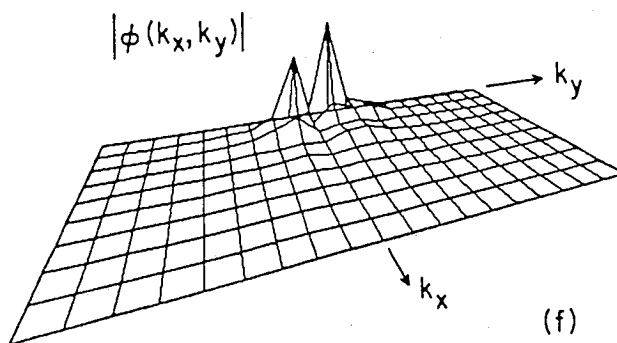
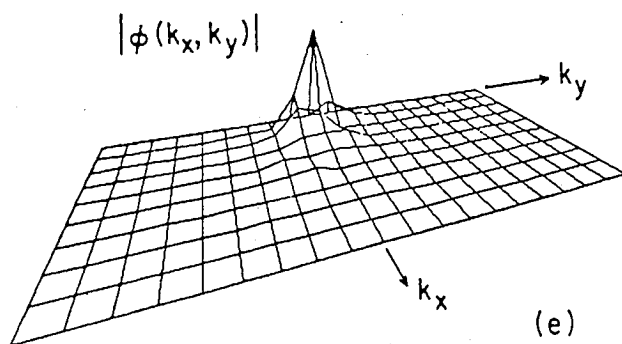


Fig. 8(e)-(h)